Joint constraints on the field-cluster mixing fraction, common envelope efficiency, and globular cluster radii from a population of binary hole mergers via deep learning

Kaze W. K. Wong, Katelyn Breivik, Kyle Kremer, and Thomas Callister

Joint constraints on the field-cluster mixing fraction, common envelope efficiency, and globular cluster radii from a population of binary hole mergers via deep learning

Kaze W. K. Wong,[1, *] Katelyn Breivik,[2] Kyle Kremer,[3, 4] and Thomas Callister[2]

[1] *Department of Physics and Astronomy, Johns Hopkins University, 3400 N. Charles Street, Baltimore, MD 21218, USA*
[2] *Center for Computational Astrophysics, Flatiron Institute, New York, NY 10010, USA*
[3] *TAPIR, California Institute of Technology, Pasadena, CA 91125, USA*
[4] *The Observatories of the Carnegie Institution for Science, Pasadena, CA 91101, USA*

The recent release of the second Gravitational-Wave Transient Catalog (GWTC-2) has increased significantly the number of known GW events, enabling unprecedented constraints on formation models of compact binaries. One pressing question is to understand the fraction of binaries originating from different formation channels, such as isolated field formation versus dynamical formation in dense stellar clusters. In this paper, we combine the `COSMIC` binary population synthesis suite and the `CMC` code for globular cluster evolution to create a mixture model for black hole binary formation under both formation scenarios. For the first time, these code bodies are combined self-consistently, with `CMC` itself employing `COSMIC` to track stellar evolution. We then use a deep-learning enhanced hierarchical Bayesian analysis to continuously sample over and constrain the common envelope efficiency α assumed in `COSMIC`, the initial cluster virial radius r_v adopted in `CMC`, and the intrinsic mixture fraction f between each channel. Under specific assumptions about other uncertain aspects of isolated binary and globular cluster evolution, we report the median and 90% confidence interval of three physical parameters for the intrinsic population $(f, \alpha, r_v) = (0.20^{+0.32}_{-0.18}, 2.26^{+2.65}_{-1.84}, 2.71^{+0.83}_{-1.17})$. This simultaneous constraint agrees with observed properties of globular clusters in the Milky Way and is an important first step in the pathway toward learning the astrophysics of compact binary formation through GW observations.

I. INTRODUCTION

The number of gravitational-wave (GW) detections is growing at an accelerating pace since the first detection [1]. The LIGO-Virgo-KAGRA Collaboration (LVKC) recently released the second Gravitational-Wave Transient Catalog (GWTC-2), which includes 39 events from the first half of of the third observational run (O3) [2]. The number of GW events in this new catalogue (50) is ~ 4 times the number of events from the first two observational runs combined [3], allowing for the increasingly sensitive exploration of their mass, spin and merger redshift distributions [4]. As the statistical uncertainties in these distributions continue to drop with the growing number of detections, the population of GW events provides a unique, and increasingly powerful, avenue to probe a wide range of topics, including fundamental physics [5], cosmology [6, 7], and astrophysics [8–10].

One of the most pressing questions in GW population analyses is which binary formation channels generate the observed GW events. In particular, it is expected that compact binary mergers may arise via isolated binary evolution in the stellar field or dynamical assembly in dense clusters, although a variety of other channels have also been theorized [11–13]. In the isolated field scenario, compact binary mergers are the end result of stellar binary evolution [14, 15]. On the other hand, events from dynamical formation scenarios are formed through multi-body encounters in dense environments, such as globular clusters, young stellar clusters, or galactic nuclear clusters [16, 17]. While the precise distributions of compact binaries originating from each scenario are not known, field and cluster channels generally differ in their predictions regarding spin, eccentricity, and component mass distributions of binary mergers. Due to mass transfer and tidal alignment, binaries resulting from the isolated formation tend to have component spins aligned with their orbital angular momenta, whereas dynamically formed binaries are believed to have an isotropic distribution of spins [18–21]. Also, hierarchical mergers are likely only possible in a dynamical-formation scenario [22–25], which could result in black holes with masses in the theorized pair-instability supernova (PISN) gap (commonly known as the "upper mass gap") [26, 27].

Some studies have already sought to use the observed masses and spins of compact binary mergers to infer the mixing fraction between the two formation channels [4, 28, 29]. Such studies, however, generally adopt heuristic models for expected spin distributions, or ignore possible variation within individual channels that may be correlated with the inferred mixing fractions. Moreover, although the mixing fraction itself is an important question, understanding the mixing fraction alone yields little insight on the physics of each underlying formation channel. Thus, it is important to infer the mixing fraction and channel-specific parameters *jointly*. In this study, we create a mixture model of merging binary black holes (BBHs) from isolated binary evolution using the binary population synthesis code `COSMIC` and from globular clusters (GCs) using the GC evolution code `CMC`. We infer the properties of this mixture model by applying a deep learning enhanced hierarchical Bayesian modeling framework

on the GWTC-2 BBH catalogue.

The paper is structured as follows: In section II, we describe the library of COSMIC and CMC simulations used in this study. In section III, we review our data analysis pipeline that applies deep-learning to emulate and interpolate between our library, allowing for hierarchical inference of parameters governing binary formation. In section IV, we present results obtained by applying our pipeline to public data released in support of GWTC-2. Finally, in section V, we discuss implications of this work.

II. SIMULATION

A. Isolated binary evolution with COSMIC

We generate a cosmological population of BBH mergers originating from isolated binary evolution using COSMIC[30], which is based on an updated version of BSE [31]. See [30] for a comprehensive summary of all upgrades currently employed in COSMIC and [32] for a detailed discussion of the prescriptions which most heavily impact compact-object formation in biaries. We assume that massive stars are initially distributed with masses following a power law with index $\alpha = -2.3$ [33] and 70% of them have companions with mass ratios distributed uniformly [34]. [Corr: We distribute initial orbital periods with a power law in log orbital period with index $\pi = -0.55$ and $\log(P_{orb}/\text{day}) \in [0.15, 5]$ following the assumptions of [34, 35] and initial eccentricities with a power law with index $\xi = -0.45$ for $e \in [0.001, 0.9]$ [34]].

One of the largest uncertainties in binary evolution is the amount a binary's orbital separation shrinks as a result of common envelope evolution [36]. COSMIC employs the $\alpha\lambda$ prescription to parameterize how efficiently orbital energy is used in unbinding the stellar envelope, where λ is the envelope binding energy and is calculated following Appendix A of [37] assuming no contributions from ionizing energy. Previous studies suggest a wide range of ejection efficiencies varying from $\alpha = 0.25 - 5$ for a wide variety of stellar masses [e.g. 38–40]. To capture this uncertainty, we ran 8 separate models ($\alpha = 0.25, 0.5, 0.75, 1, 2, 3, 4, 5$) each with 16 metallicity bins spaced logarithmically between $Z_\odot/200$ and $2Z_\odot$, where $Z_\odot = 0.017$ [41]. The binary evolution model, except for the variation of envelope ejection efficiency, is identical to that of [32] which consistently produces local ($z < 0.01$) merger rates consistent within a factor of 2 to the 90% credible interval of the observed rates from the GWTC-1 catalog for $\alpha = 1, 5$. For a discussion of the local comoving merger rates for our simulated populations, see Sec. V.

To generate a cosmological population of merging BBHs, we use the redshift-dependent star formation history and metallicity evolution of [42] and assume *Planck 2015* cosmological parameters: $H_0 = 68$ km s^{-1} Mpc^{-1}, $\Omega_m = 0.31$ and $\Omega_\Lambda = 0.69$ [43] as implemented in astropy [44, 45]. Similar to [32], we assume a truncated log-normal distribution of metallicities with $\sigma = 0.5$ dex following

[21]. We break the star formation into 100 linearly spaced redshift bins between 0 and 14 and calculate the number of BBHs formed, weighted by their metallicity, by normalizing the total mass of stars from our simulated population to the total amount of star formation in each redshift bin. We then record the lookback time and the redshift of each BBH merger to create a catalog of all merging BBHs for redshifts $z < 15$.

B. Globular cluster evolution with CMC

We use N-body simulations presented in the CMC Cluster Catalog [46] to simulate GC evolution. These simulations were computed using CMC (for Cluster Monte Carlo) [47, 48], a Hénon-type Monte Carlo code which includes various processes relevant to BH binary formation including two-body relaxation [47], three-body binary formation [49], direct integration of small-N resonate encounters [50, 51], and stellar/binary evolution. For the latter, CMC uses updated versions of SSE and BSE [31, 52], identical to those used in COSMIC, only varying in choices of binary evolution prescriptions. [Corr: In CMC, we assume a 5% percent primordial binary fraction (uniform across all primary masses which in turn are drawn from a Kroupa [53] initial mass function over the range $0.08 - 150\,M_\odot$). We assume mass ratios are drawn from a uniform distribution in range $[0.1 - 1]$. Binary orbital periods are drawn from a distribution flat in log-scale, with the orbital separations ranging from near contact ($a \geq 5(R_1 + R_2)$, where R_1 and R_2 are the stellar radii) to the hard/soft boundary of the cluster (reflecting the fact that soft binaries are expected to be broken quickly through dynamical encounters). Additionally, we assume initial eccentricities are drawn from a thermal distribution [e.g., 54].]

In the CMC Cluster Catalog, four key cluster parameters are varied between the different simulations: initial number of stars per cluster ($N/10^5 = 2, 4, 8, 16$), initial virial radius ($r_v/\text{pc} = 0.5, 1, 2, 4$), metallicity ($Z/Z_\odot = 0.01, 0.1, 1$), and radial position within a (Milky-Way-like) galactic potential ($R_{gc}/\text{kpc}=2,8,20$). Collectively, this simulation suite covers the full parameter space of the Milky Way GCs and captures the formation of a variety of astrophysical objects including GW sources, X-ray binaries, millisecond pulsars, and blue stragglers.

By coupling a cluster age distribution model from [55] with the BBH merger delay time distributions gathered from the CMC models, a realistic distribution of dynamical BBH merger times can be assembled. In [46], this method was used to estimate a BBH merger rate of roughly $20\,\text{Gpc}^{-3}\,\text{yr}^{-1}$ in the local universe (assuming all N, r_v, Z, and R_{gc} values are equally weighted), consistent with similar rate estimates from other recent studies [e.g., 56–58].

While COSMIC can produce nearly arbitrarily large catalogs of compact binary mergers, the output of CMC is limited by the relatively high computational costs as-

sociated with dynamical N-body simulations [e.g., 48]. As a result, the total number of GW events from our set of CMC models is of order 10^4 compared to several million from each COSMIC model. To mitigate the presence of small-scale fluctuations due to finite sampling, which may inadvertently be learned and reproduced by our emulator, we smooth the binary mass distributions given by each CMC simulation with a gaussian kernel using scipy.stats.gaussian_kde. The smoothing preserves physical features in the mass functions, such as high-mass "bumps" due to repeated mergers, while smoothing out small unwanted scale fluctuations.

C. Mixture model

In an ideal scenario, a single model would be used to simultaneously predict both the observable properties and the merger rates of compact binaries across all different formation channels. In this case, the mixing fraction between channels would be a direct prediction of the model, requiring no additional free parameters. In practice, the compact binary merger rates given by both COSMIC and CMC are highly uncertain and possibly subject to severe systematic bias. Therefore, when combining simulations to create a mixture model between field and cluster populations, we deliberately introduce a free parameter f controlling the mixing fraction:

$$
\begin{aligned}
p(m_1, m_2, z | \alpha, r_v, f) = & f p_{\mathrm{cosmic}}(m_1, m_2, z | \alpha) \\
& + (1-f) p_{\mathrm{CMC}}(m_1, m_2, z | r_v), \quad (1)
\end{aligned}
$$

where $p_{\mathrm{cosmic}}(m_1, m_2, z)$ and $p_{\mathrm{CMC}}(m_1, m_2, z)$ are the probability densities on the primary mass m_1, secondary mass $m_2 \leq m_1$, and redshift z of BBH mergers predicted by COSMIC and CMC, respectively. This choice of mixture model ensures that our conclusions are physically informed by the *shapes* of the observed mass and redshift distributions, and not on the *rates* of binary mergers. The parameters of the mixture model are summarized in table I.

TABLE I. Event parameters and hyper-parameters used in this work.

Event parameters $\boldsymbol{\theta}$	
$m_1 \in [2.5, 100]\ M_\odot$	Source-frame primary mass of the binary
$m_2 \in [2.5, 100]\ M_\odot$	Source-frame secondary mass of the binary
$z \in [0, 1.2]$	Redshift of the binary
Hyper-parameters $\boldsymbol{\lambda}$	
$\alpha \in [0.25, 5]$	Common envelope efficiency
$r_v \in [0.5, 4]$ pc	Initial cluster virial radius
$f \in [0, 1]$	Fraction of binaries from field-formation channel

Each combination of hyper-parameters generically yields a different distribution of primary masses and mass ratios ($q = m_2/m_1$). Several different examples are shown in Fig. 1, varying the common envelope efficiency α in COSMIC (left-hand side) and the initial cluster virial radius r_v in CMC (right-hand side). Larger common envelope efficiencies, for instance, produce relatviely lower primary masses, while clusters with larger r_v retain more massive BHs at late times and thus exhibit the high-mass peak around $80\,M_\odot$ due to repeated BH mergers.

The shift towards lower primary masses with increasing common envelope ejection efficiency is a result of increased rates of mergers during the common envelope phase, before a BBH forms. COSMIC assumes that BH mass is directly correlated with progenitor mass, thus lower mass BHs will have lower mass stellar progenitors which enter common envelopes in closer orbits relative to higher mass BHs and progenitors. Since the delay times for merging BBHs in all of our models which originate from post-common-envelope binaries are short enough for the majority of the population to merge within a few Gyr at most (even with $\alpha = 5$), the mergers of progenitors which would form lower mass BHs is the dominant effect which shapes the black hole primary mass spectrum. We note that Fig. 1 shows the probability distribution in primary mass, thus direct comparisons of histogram height do not reflect the absolute contributions of model to the overall rate of merging BBHs.

In the CMC models, the BH mass spectrum features three prominent peaks: the first at roughly $10 - 20\,M_\odot$ due to the assumptions concerning mass fallback during core collapse [e.g., 59], the second at roughly $40\,M_\odot$ due to the assumptions concerning the pair-instability [e.g., 60], and the third at roughly $70 - 80\,M_\odot$ due to first-generation-BH-merger products retained in their host cluster post-merger [e.g., 24]. The first two peaks are similarly found in the COSMIC models (as expected, given these peaks are features of single star evolution assumptions), while the third peak is unique to the dynamical cluster environment. The shift toward higher primary masses at higher r_v is a consequence of the effect of r_v on BH cluster dynamics. Primarily due to mass segregation arguments, the most massive BHs in a cluster will, on average, be the first to be ejected from their host cluster and merge [e.g., 46, 49]. The lower-mass ($\approx 10 - 15\,M_\odot$) BHs become dynamically active only after the most massive BHs have been ejected. For smaller initial r_v, high-mass BHs are dynamically processed and ejected early on. Therefore, in these clusters, high-mass ($M \gtrsim 40 M_\odot$) BHs, including the second-generation BHs with masses in the pair-instability gap, typically merge at high redshift leaving only the least massive BHs in any significant quantity at late times (low redshift). Meanwhile, for high-r_v clusters, the initial relaxation time is longer [e.g., 61], so many high-mass BHs still remain and may merge at late times. Thus, BBH mergers tend to have higher component masses for higher r_v clusters, as shown in Fig. 1.

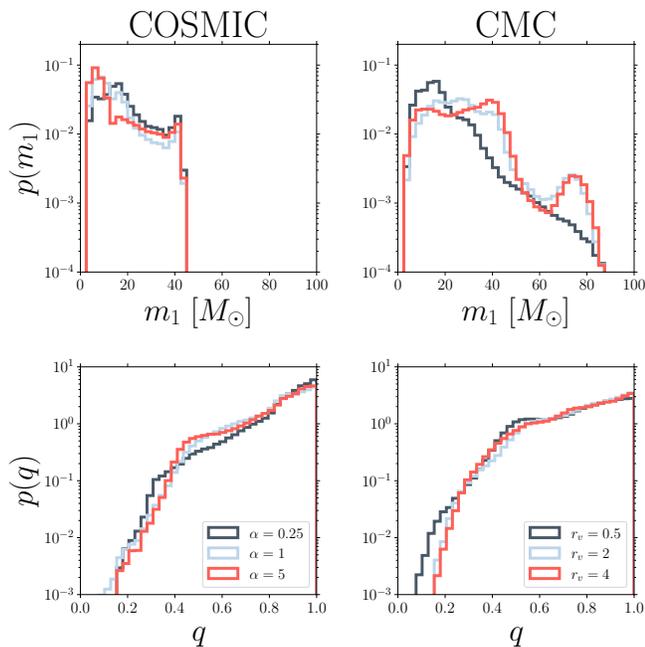The most significant difference between the two forma-

FIG. 1. Distributions of source-frame primary mass and mass ratio for all merging BBHs from the COSMIC and CMC models. The left column shows the distributions for different common envelope efficiencies and merging BBHs from COSMIC only, and the right column shows the distributions for different initial virial radii when we only consider BBH mergers from CMC.
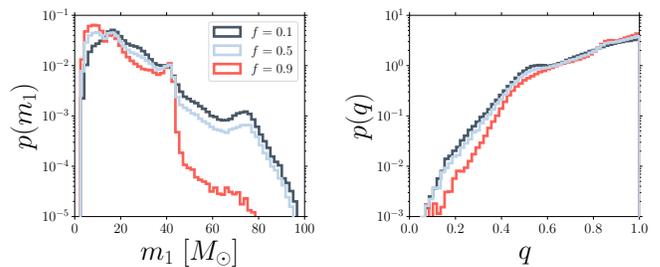

FIG. 2. The source-frame primary mass and mass ratio distribution for all merging BBHs in the mixture model. We fixed $\alpha = 1$ and $r_v = 1$ then mix the distributions with three values of the mixing fraction $f = [0.1, 0.5, 0.9]$

III. METHOD

In this section, we give a brief summary of the hierarchical inference and deep learning methods used in this work. We refer the readers to the comprehensive descriptions in e.g. Refs [62–64] for additional details.

Given data $\boldsymbol{d}$ spanning a number N_{obs} of gravitational-wave detections, we wish to infer the posterior $p(\boldsymbol{\lambda}|\boldsymbol{d})$ on the hyperparameters $\boldsymbol{\lambda}$ governing their population. Assuming that the population is described as an inhomogenous Poisson process, the posterior takes the form [64, 65]

$$p(\boldsymbol{\lambda}|\boldsymbol{d}) \propto \pi(\boldsymbol{\lambda}) e^{-\alpha(\boldsymbol{\lambda})N(\boldsymbol{\lambda})} N(\boldsymbol{\lambda})^{N_{\text{obs}}}$$
$$\times \prod_{i=1}^{N_{\text{obs}}} \int \frac{p(\boldsymbol{d}|\boldsymbol{\theta}_i)\, p_{\text{pop}}(\boldsymbol{\theta}_i|\boldsymbol{\lambda})}{\alpha(\boldsymbol{\theta}_i)} d\boldsymbol{\theta}_i, \qquad (2)$$

where $N(\boldsymbol{\lambda})$ is the intrinsic volume-integrated event rate predicted by the model, and N_{obs} is the number of observed event in the data. $p(\boldsymbol{d}|\boldsymbol{\theta}_i)$ is the likelihood of the i-th event in the observed catalogue and $\pi(\boldsymbol{\lambda})$ is the prior on our hyperparameters. Meanwhile, $p_{\text{pop}}(\boldsymbol{\theta}_i|\boldsymbol{\lambda})$ is the probability density function for the event-level parameters $\boldsymbol{\theta}_i$; this function will be computed using a normalizing flow emulator.

The term $\alpha(\boldsymbol{\lambda})$ is known as the selection bias, and gives the fraction of events one expects to detect:

$$\alpha(\boldsymbol{\lambda}) = \int p_{\text{pop}}(\boldsymbol{\theta}'|\boldsymbol{\lambda}) P_{\text{det}}(\boldsymbol{\theta}') d\boldsymbol{\theta}'. \qquad (3)$$

where $P_{\text{det}}(\boldsymbol{\theta}')$ is the probability that an event with specific parameters $\boldsymbol{\theta}'$ is successfully detected. In principle, one needs to inject a large amount of signals and recover them with a search pipeline to estimate the selection bias, which is very computationally expensive. In practice, we follow the procedure described in [4, 66], reweighting an injection campaign done by the LVKC to compute the selection bias for the O12 + O3a catalog. We interpolate $N(\boldsymbol{\lambda})$ and $\alpha(\boldsymbol{\lambda})$ and use the interpolated function during the inference to maximize computational efficiency.

As discussed above, the absolute merger rates predicted by the COSMIC and CMC simulations are likely subject to

tion channels is the existence or absence of black holes in the upper mass gap, with $m_1 \gtrsim 45\,M_\odot$. All stars in our simulations, including those formed in GCs, are subject to PISNe which results in a sharp mass cutoff near $m_1 \approx 45\,M_\odot$ for all first generation BBH mergers. We note that the assumptions for neutrino mass loss in our COSMIC and CMC models differ slightly such that the maximum mass for a first generation BBH component is $44.5\,M_\odot$ in COSMIC and $40.5\,M_\odot$ in CMC. This difference arises in the choice for neutrino mass loss to carry away a fixed $0.5\,M_\odot$ or 10% of the compact object mass at formation. Only hierarchical mergers, which do not occur in our isolated binary simulations, can result in BBHs with masses polluting the upper mass gap. This fact serves as the primary means of disentangling formation channels and measuring their mixing fraction f. Figure 2, for example, shows the *total* m_1 and q distributions resulting from combining field and cluster channels, assuming $alpha = 1$ and $r_v = 1$ for several different mixing fractions f, the exact value of which sensitively controls the prevalence of high-mass systems. Thus the relative numbers of high- and low-mass binaries among GWTC-2 serves as a sensitive probe of the true value of f.

unknown systematic uncertainties. We therefore marginalize the posterior shown in Eq.(2) over the intrinsic merger rate, using a prior $\pi(N) \propto 1/N$. Additionally, we do not know the underlying likelihood $p(\boldsymbol{d}|\boldsymbol{\theta}_i)$ for each catalog event, but only the *posterior* $p(\boldsymbol{\theta}_i|\boldsymbol{d})$ obtained under some default prior $\pi(\boldsymbol{\theta}_i)$ adopted by the LVKC during parameter estimation. Under both of these conditions, Eq. (2) can be written as [67]

$$p(\boldsymbol{\lambda}|\boldsymbol{d}) \propto \pi(\boldsymbol{\lambda}) \prod_{i=1}^{N_{\mathrm{obs}}} \int \frac{p(\boldsymbol{\theta}_i|\boldsymbol{d})}{\pi(\boldsymbol{\theta}_i)} \frac{p_{\mathrm{pop}}(\boldsymbol{\theta}_i|\boldsymbol{\lambda})}{\alpha(\boldsymbol{\lambda})} \mathrm{d}\boldsymbol{\theta}_i . \quad (4)$$

Specifically, the LVKC releases their event posterior in the form of discrete samples produced by their parameter estimation pipeline. Given these samples, the integral in Eq. (4) can be evaluated by using importance sampling, which turns the integral into a discrete sum over the event posterior PDF samples

$$p(\boldsymbol{\lambda}|\boldsymbol{d}) \propto \pi(\boldsymbol{\lambda}) \prod_{i=1}^{N_{\mathrm{obs}}} \frac{1}{S_i} \sum_{j=1}^{S_i} \frac{p_{\mathrm{pop}}(^j\boldsymbol{\theta}_i|\boldsymbol{\lambda})}{\pi(^j\boldsymbol{\theta}_i)\alpha(\boldsymbol{\lambda})}. \quad (5)$$

where j labels the posterior samples of the i-th event and S_i is the total number of samples per event. The default prior used in the LVKC `LALInference` software [68] is uniform in *detector-frame* masses and quadratic in luminosity distance, whereas we wish to model the distributions of source-frame masses and redshifts. In terms of these desired coordinates, the `LALInference` prior takes the form

$$\pi(m_1, m_2, z) \propto (1+z)^2 D_L^2(z) \left(D_c(z) + \frac{c(1+z)}{H(z)} \right) . \quad (6)$$

To evaluate Eq. (5), we make use of the posterior samples presented in Refs. [3] and [2] and released through the Gravitational-Wave Open Science Center [69]. In particular, we use the "`PublicationSamples`" dataset associated with each event, and restrict to the 44 events with false alarm rates $< 1\,\mathrm{yr}^{-1}$ following Ref. [4].

The final term we need for evaluating Eq. (5) is the distribution of observables predicted by our simulation $p_{\mathrm{pop}}(\boldsymbol{\theta}|\boldsymbol{\lambda})$, which we obtain through training a deep learning emulator on the simulations. Here we give the network-related hyperparameters for reproducing our result. A detailed discussion of the architecture of the neural network and of the training procedure can be found in Refs. [62, 63]. We train a masked autoregressive flow network [70] with 10 hidden layers, each layer having 1024 units with ReLU activation. We include 3 observables $\{m_1, m_2, z\}$ and 3 hyper-parameters $\{f, \alpha, r_v\}$ in our training, as tabulated in Table I. The training set contains 160 simulations with different combinations of 8 values of $\alpha \in [0.25, 5]$, 4 values of $r_v \in [0.5, 4]$ and 5 values of $f \in [0, 1]$. Each simulation has 10^5 events, of which 80% are randomly chosen our training set and 10% for both validation and test sets. Note that we follow the LVKC convention to enforce

$m_1 > m_2$. We train the network for 100 epoch on a Nvidia K80 GPU to ensure convergence. The code for the neural network is written in python with PYTORCH [71]. Eq. (5) is then sampled using the MCMC package `emcee` [72] to produce the results shown in this work.

IV. RESULT

We infer the hyper-parameters of Eq. (1) using the posterior samples publicly released in support of GWTC-1 [3, 73] and GWTC-2 [2, 74], restricting to the 44 events with false alarm rates $< 1\,\mathrm{yr}^{-1}$. Our main results are shown in Fig. 3. As shown in Fig. 1, a component mass larger than $\sim 45\,M_\odot$ is a signature of GC-formed BBHs [Corr: within our two-channel model]. In GWTC-1, only GW170729 has a source-frame primary mass estimate with a median larger than $45\,M_\odot$. With only 10 events in GWTC-1, the mixing fraction is therefore rather unconstrained, and the data show a preference for a near-equal mixing of the two populations instead of one dominating the other (grey $1-$D histograms). This is not the case for GWTC-2. There are 8 events with median source-frame primary masses $> 45\,M_\odot$. Together with the events from GWTC-1, 9 out of 44 events pass the PISN mass gap. This boost in number of high mass events significantly shifts the preferred value of the mixing fraction toward the cluster formation scenario. [Corr: For comparison, if we ignore the 9 events in the PISN mass gap, the inferred mixing fraction becomes $0.5^{+0.4}_{-0.28}$.] Despite this preference for cluster formation, the field formation scenario can still contribute significantly to the entire observed population. Our 90% credible upper bound on the mixing fraction is $f = 0.522$ suggesting that the contribution from the isolated channel could still surpass the cluster formation channel.

Our posterior on the common envelope efficiency α shows a mild preference towards lower values. Our relative insensitivity to α is due to two effects. First, varying α changes the mass distributions predicted by `COSMIC` by only a factor of a few, [Corr: so one need more events for the difference in distribution with difference α to become statistically significant.] Second, since the mixing fraction favours the cluster formation channel over the isolated formation channel, the effective number of events which was used to constrained the common envelope efficiency is even smaller.

In contrast, the initial cluster virial radius r_v is reasonably well-constrained, since our module suggests that more BBH mergers originate in GCs than in isolation. There are 5 events with a component mass larger than $60\,M_\odot$, which make up more than 10% of the entire dataset. As clusters with larger initial virial radii tend to yield more massive mergers at higher redshift (including hierarchical mergers with masses in the pair-instability gap), the excess of high-mass events hints that the majority of clusters may have been born with moderately large virial radius (we predict a median value of $2.71\,\mathrm{pc}$).
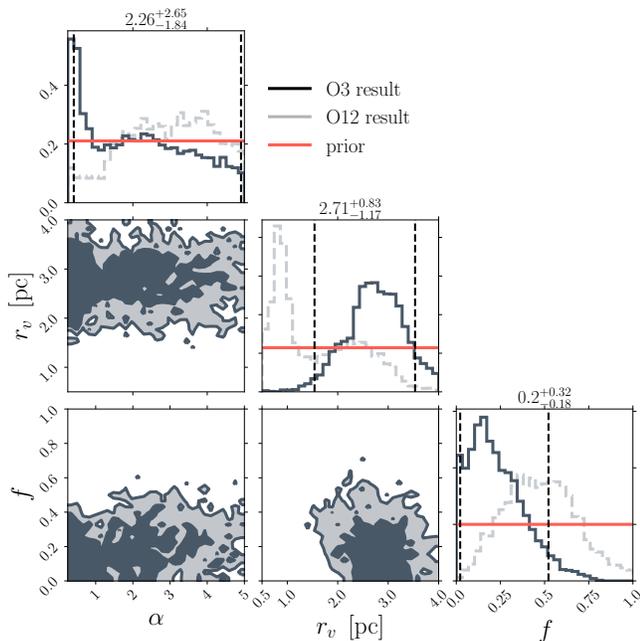
FIG. 3. The posterior distribution of our model inferred by using all BBHs up to GWTC-2. The contours represent 50% and 90% credible bounds. The grey lines in the 1D marginalized results are posterior distribution inferred by using only BBHs in GWTC-1.

[Corr: We also find the constraint on r_v correlates with f mildly. By taking a thin bin of posterior samples with $f = 0$, we found the median and standard deviation of r_v are $(2.79, 0.44)$; With $f = 0.5$, the median and standard deviation of r_v are $(2.65, 0.64)$. While the shift of median is rather insignificant, the posterior distribution is less constrained when mixed with COSMIC ($f > 0$) because we have less effective events to constrain CMC.]

Figure 4 shows our inferred primary mass distribution, marginalized over our posterior on f, α, and r_v. For comparison, the light blue band indicates the mass spectrum inferred by the LVC using their phenomenological "Multi-Peak" model, where the primary mass distribution is modeled as the superposition of a power law with two additional Gaussians that can capture the onset of pair instability and the presence of high-mass hierarchical mergers, if present [4]. Despite their very different parametrizations, both models yield qualitatively similar structure at moderate and high masses: a steep drop near $\sim 45\, M_\odot$ (corresponding to the onset of the pair instability mass gap in our model) followed by a plateau and possible secondary peak near $80\, M_\odot$ due to second-generation mergers in GCs.

V. DISCUSSION

Previous analyses [e.g., 46, 75] have shown a cluster's initial r_v plays a prominent role in the cluster's long-
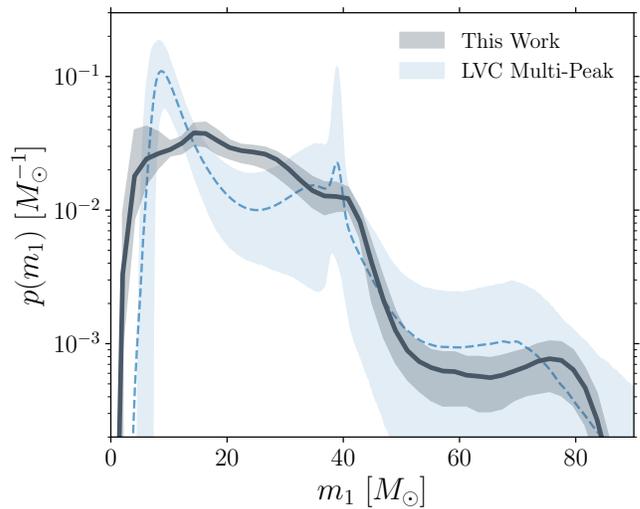

FIG. 4. The primary mass distribution (shaded grey) inferred by our mixture model. Specifically, the shaded band shows the central 90% credible bound on $p(m_1)$ as a function of primary mass, while the solid line marks the population predictive distribution: the inferred probability distribution on m_1 after marginalization over the field-cluster mixing fraction f, common envelope efficiency α, and initial cluster virial radius r_v. For comparison, the shaded blue band marks the analogous result obtained by the LVC under their "Multi-Peak" mass model; the dashed blue line is the corresponding population predictive distribution.

term dynamical evolution. In particular, GCs born with smaller initial r_v (and thus shorter relaxation times), are more likely to have undergone core collapse by the present day. In this case, the relative ratio of core-collapsed to non-core-collapsed GCs observed at present may provide a complementary constraint upon the initial r_v distribution [46]. Taking the Milky Way GCs as a representative sample, roughly 80% of clusters have well-resolved cores (i.e., are non-core-collapsed) at present [76], potentially hinting that relatively large initial r_v are typical, consistent with the predictions from our GWTC-2 inference.

There are a number of assumptions made in this work that can be improved upon in the future. To safeguard against systematic model uncertainties, we do not include merger rates in our inference. For completeness, we report the comoving merger rate at $z < 0.1$ under each formation channel and hyper-parameter choice in Table II. The local merger rates from the isolated formation channel are lie near the maximum value of the 90% confidence intervals of the reported merger rates inferred from GWTC-2 of $23.9^{+14.9}_{-8.6}\, \mathrm{Gpc}^{-3}\, \mathrm{yr}^{-1}$. This illustrates a potential systematic bias in the other parameters which define the isolated binary formation models. In particular, COSMIC assumes that natal kicks for BHs are drawn from a Maxwellian distribution with $\sigma = 265\, \mathrm{km/s}$ and then weighted by the amount of mass that falls back onto the proto-compact-object during formation [59]. If stronger kicks are assumed, BBHs with lower masses will

TABLE II. Event rates for each hyper-parameter and formation scenario. Rates are given for $z < 0.1$ and in comoving volume per time.

Isolated binaries								
α	0.25	0.5	0.75	1	2	3	4	5
Γ_α [Gpc^{-3}yr^{-1}]	63.8	62.5	66.5	72.2	76.6	75.1	73.9	72.1

Globular clusters				
r_v [pc]	0.5	1	2	4
Γ_{r_v} [Gpc^{-3}yr^{-1}]	31.6	26.8	20.9	8.7

preferentially be unbound, altering both the merger rate and mass distributions in the isolated formation scenario [e.g. 62, 77, 78]. COSMIC also assumes that stable Roche-overflow mass transfer is conservative, which may over predict the orbital evolution of a mass transferring binary [e.g. 79].This is further compounded by our uncertain choice, following [80], of the mass ratios for which mass transfer is assumed to be dynamically unstable leading to a common envelope. If mass transfer proceeds stably for a wider range of mass ratios, fewer systems will experience dramatic orbital tightening during common envelope, potentially lowering predicted merger rates. We leave a full study of the combined effects of BH natal kicks, common envelope, mass transfer stability, and accretion efficiency to a future study.

Although the rate estimates from clusters shown in Table II match well the reported comoving rate inferred from GWTC-2, the cluster estimates also feature several uncertainties. A major uncertainty is the assumed cluster formation history. Observations of young stellar clusters in the local universe [e.g., 81] indicate that initial cluster virial radii are roughly independent of cluster birth time and metallicity, however this is highly uncertain. If r_v does vary with cluster birth time, it may substantially affect the conclusions of this study. Furthermore, the cluster birth time distribution itself is highly uncertain. Current theories of cluster formation fall into two main categories: clusters formed through active star formation [e.g., 55, 82] and clusters formed due to the collapse of dark matter halos during or before the epoch of reionization [e.g., 83]. Here, we have assumed the former scenario but if a large population of present-day GCs were instead born during reionization, our results may again change significantly. Future work should consider more carefully the various possible assumptions regarding cluster formation scenarios and the dependence of cluster properties such as r_v on these various scenarios.

There are many valuable routes by which this present analysis may be expanded in the future. As features in the BBH spin distribution begin to be robustly resolved [4, 84–88], future analyses can incorporate spin measurements alongside mass and redshift. Future measurements of orbital eccentricity may additionally help to discriminate between formation scenarios [51, 89, 90]. Finally, due to

the still moderate number of events, in this work we restricted purely to BBHs and considered only CE and GC formation, neglecting other proposed formation channels such as primordial BHs, nuclear star clusters, open clusters, stellar triples, and AGN disks; future analysis can incorporate a greater diversity of formation scenarios, as in Ref. [88], and seek to self-consistently include neutron star and neutron star-black hole binaries alongside BBHs. We note that our results, which favor BBH formation in GCs, are in slight tension with those of Ref. [88], which identifies a preference for CE evolution. This tension may be due to a number of differences in the underlying models and data analysis methods used, including the methods for estimating selection effects (we adopt a pipeline-based false alarm threshold, compared to the optimal signal-to-noise threshold employed in Ref. [91]), the number of formation channels considered, the broader coverage of r_v in our CMC models (our inferred value of $r_v \approx 2.7$ pc is outside the r_v range considered in Ref. [91]), and our unique ability to continuously sample over otherwise discretized parameters like α and r_v.

To conclude, we have extracted the mixing fraction of BBHs formed in isolated binaries and GCs while simultaneously placing continuous constraints on the channel-specific hyper-parameters, notably the initial virial radius of GCs where the BBHs were formed. Our work marks an important milestone of learning astrophysics from populations of observed GW events. Instead of constraining a physics-agnostic phenomenological model, we use a population of GW events to place constraints on physical parameters such as mixing fraction directly. Furthermore, our model suggests that the GC properties inferred from the detected GW population are consistent with electromagnetic observations of present-day GCs, notably cluster core radii distributions. This result may be readily compared with other independent measurements to test theories of GC formation and evolution. As the number of GW detections increases in the future and theoretical models improve, one can apply the same methodology to discover and test a plethora of astrophysical theories more precisely.

[1] B. P. Abbott *et al.* (LIGO Scientific, Virgo), Phys. Rev. Lett. **116**, 061102 (2016), arXiv:1602.03837 [gr-qc].

[2] R. Abbott *et al.* (LIGO Scientific, Virgo), (2020), arXiv:2010.14527 [gr-qc].

[3] B. P. Abbott *et al.* (LIGO Scientific, Virgo), Phys. Rev. **X9**, 031040 (2019), arXiv:1811.12907 [astro-ph.HE].

[4] R. Abbott *et al.* (LIGO Scientific, Virgo), (2020), arXiv:2010.14533 [astro-ph.HE].

[5] R. Abbott *et al.* (LIGO Scientific, Virgo), (2020), arXiv:2010.14529 [gr-qc].

[6] B. P. Abbott *et al.* (LIGO Scientific, Virgo), (2019), arXiv:1908.06060 [astro-ph.CO].

[7] A. Palmese *et al.* (DES), Astrophys. J. **900**, L33 (2020), arXiv:2006.14961 [astro-ph.CO].

[8] R. Farmer, M. Renzo, S. de Mink, M. Fishbach, and S. Justham, Astrophys. J. **902**, L36 (2020), arXiv:2006.06678 [astro-ph.HE].

[9] Y. Bouffanais, M. Mapelli, F. Santoliquido, N. Giacobbo, G. Iorio, and G. Costa, (2020), arXiv:2010.11220 [astro-ph.HE].

[10] T. Callister, M. Fishbach, D. Holz, and W. Farr, Astrophys. J. Lett. **896**, L32 (2020), arXiv:2003.12152 [astro-ph.HE].

[11] S. Bird, I. Cholis, J. B. Muñoz, Y. Ali-Haïmoud, M. Kamionkowski, E. D. Kovetz, A. Raccanelli, and A. G. Riess, Physical Review Letters **116** (2016), 10.1103/PhysRevLett.116.201301.

[12] F. Antonini, C. L. Rodriguez, C. Petrovich, and C. L. Fischer, Monthly Notices of the Royal Astronomical Society: Letters **480**, L58 (2018).

[13] B. McKernan, K. E. Saavik Ford, J. Bellovary, N. W. C. Leigh, Z. Haiman, B. Kocsis, W. Lyra, M.-M. Mac Low, B. Metzger, M. O'Dowd, S. Endlich, and D. J. Rosen, The Astrophysical Journal **866**, 66 (2018).

[14] M. Dominik, K. Belczynski, C. Fryer, D. Holz, E. Berti, T. Bulik, I. Mandel, and R. O'Shaughnessy, Astrophys. J. **759**, 52 (2012), arXiv:1202.4901 [astro-ph.HE].

[15] K. Belczynski *et al.*, Astron. Astrophys. **636**, A104 (2020), arXiv:1706.07053 [astro-ph.HE].

[16] C. L. Rodriguez, P. Amaro-Seoane, S. Chatterjee, and F. A. Rasio, Phys. Rev. Lett. **120**, 151101 (2018), arXiv:1712.04937 [astro-ph.HE].

[17] U. N. Di Carlo, N. Giacobbo, M. Mapelli, M. Pasquato, M. Spera, L. Wang, and F. Haardt, Mon. Not. Roy. Astron. Soc. **487**, 2947 (2019), arXiv:1901.00863 [astro-ph.HE].

[18] C. L. Rodriguez, M. Zevin, C. Pankow, V. Kalogera, and F. A. Rasio, Astrophys. J. Lett. **832**, L2 (2016), arXiv:1609.05916 [astro-ph.HE].

[19] W. M. Farr, S. Stevenson, M. Coleman Miller, I. Mandel, B. Farr, and A. Vecchio, Nature **548**, 426 (2017), arXiv:1706.01385 [astro-ph.HE].

[20] Y. Qin, T. Fragos, G. Meynet, J. Andrews, M. Sørensen, and H. Song, Astron. Astrophys. **616**, A28 (2018), arXiv:1802.05738 [astro-ph.SR].

[21] S. S. Bavera, T. Fragos, Y. Qin, E. Zapartas, C. J. Neijssel, I. Mandel, A. Batta, S. M. Gaebel, C. Kimball, and S. Stevenson, A&A **635**, A97 (2020), arXiv:1906.12257 [astro-ph.HE].

[22] D. Gerosa and E. Berti, Phys. Rev. **D95**, 124046 (2017), arXiv:1703.06223 [gr-qc].

[23] Z. Doctor, D. Wysocki, R. O'Shaughnessy, D. E. Holz, and B. Farr, (2019), 10.3847/1538-4357/ab7fac, arXiv:1911.04424 [astro-ph.HE].

[24] C. L. Rodriguez, M. Zevin, P. Amaro-Seoane, S. Chatterjee, K. Kremer, F. A. Rasio, and C. S. Ye, Phys. Rev. **D100**, 043027 (2019), arXiv:1906.10260 [astro-ph.HE].

[25] B. McKernan, K. E. S. Ford, R. O'Shaugnessy, and D. Wysocki, MNRAS **494**, 1203 (2020), arXiv:1907.04356 [astro-ph.HE].

[26] S. Woosley, Astrophys. J. **836**, 244 (2017), arXiv:1608.08939 [astro-ph.HE].

[27] R. Farmer, M. Renzo, S. de Mink, P. Marchant, and S. Justham, (2019), 10.3847/1538-4357/ab518b, arXiv:1910.12874 [astro-ph.SR].

[28] Y. Bouffanais, M. Mapelli, D. Gerosa, U. N. Di Carlo, N. Giacobbo, E. Berti, and V. Baibhav, Astrophys. J. **886** (2019), 10.3847/1538-4357/ab4a79, arXiv:1905.11054 [astro-ph.HE].

[29] M. Safarzadeh, Astrophys. J. Lett. **892**, L8 (2020), arXiv:2003.02764 [astro-ph.HE].

[30] K. Breivik, S. Coughlin, M. Zevin, C. L. Rodriguez, K. Kremer, C. S. Ye, J. J. Andrews, M. Kurkowski, M. C. Digman, S. L. Larson, and F. A. Rasio, ApJ **898**, 71 (2020), arXiv:1911.00903 [astro-ph.HE].

[31] J. R. Hurley, C. A. Tout, and O. R. Pols, MNRAS **329**, 897 (2002), astro-ph/0201220.

[32] M. Zevin, M. Spera, C. P. L. Berry, and V. Kalogera, ApJ **899**, L1 (2020), arXiv:2006.14573 [astro-ph.HE].

[33] P. Kroupa, MNRAS **322**, 231 (2001), arXiv:astro-ph/0009005 [astro-ph].

[34] H. Sana, S. E. de Mink, A. de Koter, N. Langer, C. J. Evans, M. Gieles, E. Gosset, R. G. Izzard, J. B. Le Bouquin, and F. R. N. Schneider, Science **337**, 444 (2012), arXiv:1207.6397 [astro-ph.SR].

[35] M. Renzo, E. Zapartas, S. E. de Mink, Y. Götberg, S. Justham, R. J. Farmer, R. G. Izzard, S. Toonen, and H. Sana, A&A **624**, A66 (2019), arXiv:1804.09164 [astro-ph.SR].

[36] N. Ivanova, S. Justham, X. Chen, O. De Marco, C. L. Fryer, E. Gaburov, H. Ge, E. Glebbeek, Z. Han, X. D. Li, G. Lu, T. Marsh, P. Podsiadlowski, A. Potter, N. Soker, R. Taam, T. M. Tauris, E. P. J. van den Heuvel, and R. F. Webbink, A&A Rev. **21**, 59 (2013), arXiv:1209.4302 [astro-ph.HE].

[37] J. S. W. Claeys, O. R. Pols, R. G. Izzard, J. Vink, and F. W. M. Verbunt, A&A **563**, A83 (2014), arXiv:1401.2895 [astro-ph.SR].

[38] M. Zorotovic, M. R. Schreiber, B. T. Gänsicke, and A. Nebot Gómez-Morán, A&A **520**, A86 (2010), arXiv:1006.1621 [astro-ph.SR].

[39] O. De Marco, J.-C. Passy, M. Moe, F. Herwig, M.-M. Mac Low, and B. Paxton, MNRAS **411**, 2277 (2011), arXiv:1010.4374 [astro-ph.SR].

[40] T. Fragos, J. J. Andrews, E. Ramirez-Ruiz, G. Meynet, V. Kalogera, R. E. Taam, and A. Zezas, ApJ **883**, L45 (2019), arXiv:1907.12573 [astro-ph.HE].

[41] N. Grevesse and A. J. Sauval, Space Sci. Rev. **85**, 161 (1998).

[42] P. Madau and T. Fragos, ApJ **840**, 39 (2017), arXiv:1606.07887 [astro-ph.GA].

[43] P. A. Ade *et al.* (Planck Collaboration), A&A **594**, A13 (2016), arXiv:1502.01589.

[44] Astropy Collaboration, T. P. Robitaille, E. J. Tollerud, *et al.*, A&A **558**, A33 (2013), arXiv:1307.6212 [astro-ph.IM].

[45] Astropy Collaboration, A. M. Price-Whelan, B. M. SipHocz, *et al.*, AJ **156**, 123 (2018), arXiv:1801.02634 [astro-ph.IM].

[46] K. Kremer, C. S. Ye, N. Z. Rui, N. C. Weatherford, S. Chatterjee, G. Fragione, C. L. Rodriguez, M. Spera, and F. A. Rasio, ApJS **247**, 48 (2020), arXiv:1911.00018 [astro-ph.HE].

[47] K. J. Joshi, F. A. Rasio, S. P. Zwart, and S. Portegies Zwart, The Astrophysical Journal **540**, 969 (2000).

[48] B. Pattabiraman, S. Umbreit, W.-k. Liao, A. Choudhary, V. Kalogera, G. Memik, and F. A. Rasio, The Astrophysical Journal Supplement Series **204**, 15 (2013).

[49] M. Morscher, B. Pattabiraman, C. Rodriguez, F. A. Rasio, and S. Umbreit, ApJ **800**, 9 (2015), arXiv:1409.0866 [astro-ph.GA].

[50] J. M. Fregeau and F. A. Rasio, apj **658**, 1047 (2007), astro-ph/0608261.

[51] C. L. Rodriguez, P. Amaro-Seoane, S. Chatterjee, and F. A. Rasio, Physical Review Letters **120**, 151101 (2018), arXiv:1712.04937 [astro-ph.HE].

[52] J. R. Hurley, O. R. Pols, and C. A. Tout, MNRAS **315**, 543 (2000), astro-ph/0001295.

[53] P. Kroupa, MNRAS **322**, 231 (2001), arXiv:astro-ph/0009005 [astro-ph].

[54] D. C. Heggie, MNRAS **173**, 729 (1975).

[55] K. El-Badry, E. Quataert, D. R. Weisz, N. Choksi, and M. Boylan-Kolchin, MNRAS **482**, 4528 (2019), arXiv:1805.03652 [astro-ph.GA].

[56] C. L. Rodriguez and A. Loeb, ApJ **866**, L5 (2018), arXiv:1809.01152 [astro-ph.HE].

[57] G. Fragione and B. Kocsis, PRL **121**, 161103 (2018), arXiv:1806.02351 [astro-ph.GA].

[58] F. Antonini and M. Gieles, arXiv e-prints , arXiv:2009.01861 (2020), arXiv:2009.01861 [astro-ph.HE].

[59] C. L. Fryer, K. Belczynski, G. Wiktorowicz, M. Dominik, V. Kalogera, and D. E. Holz, ApJ **749**, 91 (2012), arXiv:1110.1726 [astro-ph.SR].

[60] K. Belczynski, A. Heger, W. Gladysz, A. J. Ruiter, S. Woosley, G. Wiktorowicz, H. Y. Chen, T. Bulik, R. O'Shaughnessy, D. E. Holz, C. L. Fryer, and E. Berti, A&A **594**, A97 (2016), arXiv:1607.03116 [astro-ph.HE].

[61] J. Binney and S. Tremaine, *Galactic dynamics* (1987).

[62] K. W. K. Wong and D. Gerosa, Phys. Rev. **D100**, 083015 (2019), arXiv:1909.06373 [astro-ph.HE].

[63] K. W. Wong, G. Contardo, and S. Ho, Phys. Rev. D **101**, 123005 (2020), arXiv:2002.09491 [astro-ph.IM].

[64] I. Mandel, W. M. Farr, and J. R. Gair, Mon. Not. Roy. Astron. Soc. **486**, 1086 (2019), arXiv:1809.02063 [physics.data-an].

[65] T. J. Loredo, in *Bayesian Inference and Maximum Entropy Methods in Science and Engineering: 24th International Workshop on Bayesian Inference and Maximum Entropy Methods in Science and Engineering*, American Institute of Physics Conference Series, Vol. 735, edited by R. Fischer, R. Preuss, and U. V. Toussaint (2004) pp. 195–206, arXiv:astro-ph/0409387 [astro-ph].

[66] W. M. Farr, Research Notes of the American Astronomical Society **3**, 66 (2019), arXiv:1904.10879 [astro-ph.IM].

[67] M. Fishbach, D. E. Holz, and W. M. Farr, ApJ **863**, L41 (2018), arXiv:1805.10270 [astro-ph.HE].

[68] J. Veitch, V. Raymond, B. Farr, W. Farr, P. Graff, S. Vitale, B. Aylott, K. Blackburn, N. Christensen, M. Coughlin, W. Del Pozzo, F. Feroz, J. Gair, C. J. Haster, V. Kalogera, T. Littenberg, I. Mandel, R. O'Shaughnessy, M. Pitkin, C. Rodriguez, C. Röver, T. Sidery, R. Smith, M. Van Der Sluys, A. Vecchio, W. Vousden, and L. Wade, PRD **91**, 042003 (2015), arXiv:1409.7215 [gr-qc].

[69] M. Vallisneri, J. Kanner, R. Williams, A. Weinstein, and B. Stephens, in *Journal of Physics Conference Series*, Journal of Physics Conference Series, Vol. 610 (2015) p. 012021, arXiv:1410.4839 [gr-qc].

[70] G. Papamakarios, T. Pavlakou, and I. Murray, arXiv e-prints , arXiv:1705.07057 (2017), arXiv:1705.07057 [stat.ML].

[71] A. Paszke, S. Gross, S. Chintala, G. Chanan, E. Yang, Z. DeVito, Z. Lin, A. Desmaison, L. Antiga, and A. Lerer, (2017).

[72] D. Foreman-Mackey, D. W. Hogg, D. Lang, and J. Goodman, PASP **125**, 306 (2013), arXiv:1202.3665 [astro-ph.IM].

[73] LIGO Scientific Collaboration and Virgo Collaboration, (2019), https://doi.org/10.7935/KSX7-QQ51.

[74] LIGO Scientific Collaboration and Virgo Collaboration, (2019), https://dcc.ligo.org/LIGO-P2000223/public.

[75] K. Kremer, S. Chatterjee, C. S. Ye, C. L. Rodriguez, and F. A. Rasio, ApJ **871**, 38 (2019), arXiv:1808.02204 [astro-ph.GA].

[76] W. E. Harris, AJ **112**, 1487 (1996).

[77] K. Belczynski, V. Kalogera, and T. Bulik, ApJ **572**, 407 (2002), arXiv:astro-ph/0111452 [astro-ph].

[78] K. Belczynski, J. Klencki, C. E. Fields, A. Olejak, E. Berti, G. Meynet, C. L. Fryer, D. E. Holz, R. O'Shaughnessy, D. A. Brown, T. Bulik, S. C. Leung, K. Nomoto, P. Madau, R. Hirschi, E. Kaiser, S. Jones, S. Mondal, M. Chruslinska, P. Drozda, D. Gerosa, Z. Doctor, M. Giersz, S. Ekstrom, C. Georgy, A. Askar, V. Baibhav, D. Wysocki, T. Natan, W. M. Farr, G. Wiktorowicz, M. Coleman Miller, B. Farr, and J. P. Lasota, A&A **636**, A104 (2020), arXiv:1706.07053 [astro-ph.HE].

[79] L. A. C. van Son, S. E. De Mink, F. S. Broekgaarden, M. Renzo, S. Justham, E. Laplace, J. Morán-Fraile, D. D. Hendriks, and R. Farmer, ApJ **897**, 100 (2020), arXiv:2004.05187 [astro-ph.HE].

[80] K. Belczynski, V. Kalogera, F. A. Rasio, R. E. Taam, A. Zezas, T. Bulik, T. J. Maccarone, and N. Ivanova, ApJS **174**, 223 (2008), arXiv:astro-ph/0511811 [astro-ph].

[81] S. F. Portegies Zwart, S. L. W. McMillan, and M. Gieles, ARA&A **48**, 431 (2010), arXiv:1002.1961 [astro-ph.GA].

[82] J. M. D. Kruijssen, MNRAS **454**, 1658 (2015), arXiv:1509.02163 [astro-ph.GA].

[83] S. M. Fall and M. J. Rees, ApJ **298**, 18 (1985).

[84] S. Vitale, R. Lynch, R. Sturani, and P. Graff, Class. Quant. Grav. **34**, 03LT01 (2017), arXiv:1503.04307 [gr-qc].

[85] S. Stevenson, C. P. L. Berry, and I. Mandel, Mon. Not. Roy. Astron. Soc. **471**, 2801 (2017), arXiv:1703.06873 [astro-ph.HE].

[86] C. Talbot and E. Thrane, Phys. Rev. D **96**, 023012 (2017), arXiv:1704.08370 [astro-ph.HE].

[87] S. S. Bavera, T. Fragos, M. Zevin, C. P. L. Berry, P. Marchant, J. J. Andrews, S. Coughlin, A. Dotter, K. Kovlakas, D. Misra, J. G. Serra-Perez, Y. Qin, K. A. Rocha, J. Román-Garza, N. H. Tran, and E. Zapartas, arXiv e-prints , arXiv:2010.16333 (2020), arXiv:2010.16333 [astro-ph.HE].

[88] M. Zevin, S. S. Bavera, C. P. Berry, V. Kalogera, T. Fragos, P. Marchant, C. L. Rodriguez, F. Antonini, D. E. Holz, and C. Pankow, (2020), arXiv:2011.10057 [astro-ph.HE].

[89] J. Samsing, Physical Review D **97** (2018), 10.1103/physrevd.97.103014.

[90] I. M. Romero-Shaw, P. D. Lasky, and E. Thrane, Monthly Notices of the Royal Astronomical Society **490**, 5210–5216 (2019).

[91] M. Zevin, C. Pankow, C. L. Rodriguez, L. Sampson, E. Chase, V. Kalogera, and F. A. Rasio, Astrophys. J. **846**, 82 (2017), arXiv:1704.07379 [astro-ph.HE].